

Setting up a Rydberg excitation laser and stabilizing its frequency to an ultra-stable reference cavity

Aylin Cansiz

Bachelorarbeit in Physik
angefertigt im Physikalischen Institut

vorgelegt der
Mathematisch-Naturwissenschaftlichen Fakultät
der
Rheinischen Friedrich-Wilhelms-Universität
Bonn

Januar 2025

Ich versichere, dass ich diese Arbeit selbstständig verfasst und keine anderen als die angegebenen Quellen und Hilfsmittel benutzt sowie die Zitate kenntlich gemacht habe.

Bonn, ..22.01.2025..
Datum

.....Aylin Cansiz.....
Unterschrift

1. Gutachter: Prof. Dr. Sebastian Hofferberth
2. Gutachter: Prof. Dr. Stefan Linden

Acknowledgements

I would like to thank Prof. Sebastian Hofferberth for giving me the opportunity to work at the NQO group and write my thesis. The insights I got in this short time were very valuable and have taught me a lot. And I would like to thank Prof. Stefan Linden for being my second supervisor.

Furthermore, I would like to thank the whole NQO group for establishing a nice working atmosphere and the funny conversations during breaks. A special thanks goes to the HQO group, Cedric, Julia, Valerie and Sam, who have helped me a lot during my thesis. Thank you for always taking the time to explain and help me when things were not working out (and for the much needed coffee breaks).

The biggest thanks goes to my friends and especially my family, who have always helped me during a rough time and stood by my side. Your unconditional support and love have motivated me to do my best. I always wanted to make you proud and I will continue to honor the hard work and obstacles you had to go through in order to give me the opportunities you never had.

Contents

1	Introduction	1
2	The Rydberg excitation laser	3
2.1	Design and Components of the TASHGpro laser system	4
2.2	Application of the TASHGpro2 laser system in the experiment	6
3	Frequency stabilization with the Pound-Drever-Hall (PDH) Method	7
3.1	The PDH method	8
3.2	Feedback-loop and PID controller	13
3.3	Setup and results	15
4	Noise characterization with a Mach-Zehnder-Interferometer	23
4.1	Theoretical background	24
4.2	Setup and results	26
5	Conclusion and Outlook	33
	Bibliography	34
	List of Figures	38
	List of Tables	40

Introduction

When the quantum nature of light was discovered in the early 20th century, a better understanding of the atom-light interaction followed, whereas classical electrodynamics reached its limit. From then on combining the classical theories and quantum properties is conceptualized in quantum optics and lasers have become an integral device in this field [1].

Studying the interaction of photons and atoms with the help of quantum mechanics has proven to be very useful. Subsequently, the concept of absorption, spontaneous and stimulated emission with the help of level schemes were introduced, the latter being the most crucial part for a laser [2].

This opened the door to a variety of different applications, such as quantum computing, quantum communication, and quantum imaging, all achieved through quantum optics [3].

One of the interesting fields emerging from this discovery was nonlinear quantum optics (NQO), which is the focus of the NQO group of Sebastian Hofferberth in Bonn where this thesis was conducted. NQO is the study of photons interacting with photons or other quanta in the single-photon non-linear regime and the non-linear effects gain importance at high intensities [4].

Because photons do not directly interact with each other, certain tools are needed in order to create these non-linearities at a single-photon level. Thus, by using Rydberg atoms stronger photon-photon interactions are possible. Rydberg atoms are atoms in which the valence electron is excited to a much higher quantum state n than its ground state, this evokes a large dipole moment and therefore a higher sensitivity to electric fields. Another property of Rydberg atoms is the Rydberg blockade caused by the Van-der-Waals interaction between nearby Rydberg atoms shifting the required energy to excite a second Rydberg atom. This hinders the excitation of more than one Rydberg atom in a certain sphere [5].

Creating a transparent medium with the help of electromagnetically induced transparency (EIT) allows the formation of single-photon pulses because the transmission of another photon within the Rydberg blockade is suppressed [6].

I have done my research at the Hybrid Quantum Optics (HQO) experiment of the NQO group, where we aim to combine NQO with the implementation of Rydberg atoms as well as integrated photonics and optomechanical systems. In the experiment a photonic chip will be used where interactions between atoms and a microwave waveguide resonator will take place. Eventually, an electro-mechanical resonator will be coupled to the atoms for the realization of coupling between photons [7]. The realization of this project undergoes several steps. First, the Rydberg atoms are trapped in a magneto-optical trap (MOT). Then, they are excited with a probe and control field. Afterwards they are transported to the experiment region, where the actual experiment will take place. A detailed description of the experimental setup can

be found in Julia Gamper's Master thesis [8]. In the future, a cryogenic ultracold atom apparatus will allow experimental conditions at 4 K [6, 9].

For the excitation of the atoms a very precise laser system is needed in order to achieve the required transition frequencies for the experiment. This bachelor thesis focuses on the stabilization of a Rydberg excitation laser via an ultra-stable reference cavity. To do so, the Pound-Drever-Hall (PDH) method was used. Firstly, the laser system itself will be introduced in chapter 2. Secondly, the PDH method will be explained in chapter 3, with which the laser was stabilized. The frequency stabilization set up and its characterization using the error signal will also be presented in this chapter. The frequency lock was also characterized using a Mach-Zehnder-Interferometer (MZI), set up by Simon Schroers in the Rubidium Quantum Optics (RQO) lab, will be discussed in chapter 4. Lastly, a conclusion and a brief outlook will be given in chapter 5.

The Rydberg excitation laser

For the excitation of the rubidium (^{87}Rb) atoms to Rydberg states, high-precision lasers are a vital requirement. They must be able to hold a good amount of stability and have a narrow-linewidth to deliver light at specific wavelengths. [10]

In the HQO experiment the TASHGpro2 at 480 nm laser from TOPTICA can be used as the second step of the two-photon transition, after the ^{87}Rb atoms have been excited from the ground state ($5S_{1/2}$) to an intermediate state ($5P_{3/2}$) by the 780 nm probe laser [11–13]. Additionally, for continuous operation of the experiment, the need for precise control and long-term stability of the laser system gains even more importance.

The TASHGpro is a high-power, tunable, frequency-doubled diode laser and is controlled with the DLC-pro, offering less drift and better frequency stabilization [14].

First, I will provide a description of the TASHGpro laser system in section 2.1 before I move on to the application of the laser in the experiment in section 2.2.

2.1 Design and Components of the TASHGpro laser system

The TASHGpro laser system from TOPTICA Photonics is a tunable diode laser that is frequency-converted using second-harmonic generation (SHG) to provide output at 480 nm. It is composed of a tunable diode laser (DLpro), a high power semiconductor, i.e. a tapered amplifier (TA), a frequency doubling stage (SHGpro), optical isolators and control electronics. In figure 2.1 the adjustment of the different components are demonstrated.

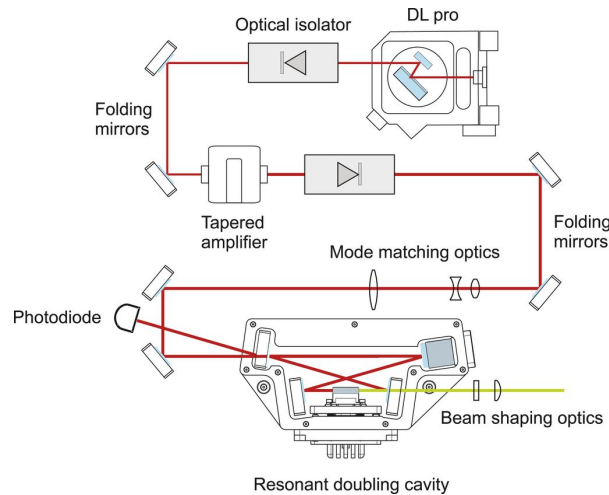


Figure 2.1: The TASHG pro system from [15] is illustrated. The seed light provided by the DLpro laser at 960 nm passes an optical isolator to prevent back reflections to the laser. Then it is guided through a TA and is then frequency doubled to 480 nm. After beam shaping optics, the light can be used in the experiment.

The tunable diode laser is an extended cavity diode laser (ECDL), which serves as the seed laser for the TASHGpro. It is designed to offer narrow linewidth and high tunability, which are crucial characteristics for experiments requiring precise control over laser frequencies. The seed laser operates at a wavelength of 960 nm and it is the source of the fundamental frequency that is later frequency-doubled in the SHG process. This wavelength is selected to optimally match the transition wavelengths of rubidium atoms for the Rydberg excitation [16].

The SHG unit is a nonlinear optical device that converts the 960 nm light from the DL Pro to 480 nm through a second-harmonic process. This process is achieved by passing the laser light through a periodically poled lithium niobate (PPLN) crystal. The PPLN crystal's periodic poling allows for phase matching, which is crucial for efficient frequency conversion [10]. Temperature stabilization of the crystal is required to maintain the efficiency of the SHG process and prevent drifts that could degrade the laser performance [17].

Optical isolators are employed in the system to prevent back reflections into reaching the diode laser. Such reflections can cause instabilities and mode hops, which would also degrade the laser's performance. By using optical isolators, the TASHGpro maintains a stable and reliable operation, ensuring that the frequency and output power remain consistent over time [17, 18].

The TASHGpro system is delivered with advanced control electronics which manage the laser's output power, wavelength tuning, and feedback mechanisms. These electronics also control the temperature of both the diode laser and the SHG crystal, ensuring that the system operates within the optimal thermal

range to maintain frequency stability [13, 19, 20].

2.2 Application of the TASHGpro2 laser system in the experiment

The TASHGpro2 laser plays a central role in the hybrid quantum optics experiments focused on Rydberg atom physics. Specifically, it is used to excite ^{87}Rb atoms to their Rydberg states through a two-photon transition process. The excitation scheme involves the following steps which are also shown in figure 2.2:

1. **First Excitation Step:** A laser at 780 nm excites the ^{87}Rb atoms from the ground state ($5S_{1/2}$) to the intermediate state ($5P_{3/2}$) [21].
2. **Second Excitation Step:** The 480 nm light from the TASHGpro2 laser further excites the atoms from the intermediate state to a high- n Rydberg state (nD or nS).

A detailed description of the probe-control setup and its characterization was done in Samuel Germer's Bachelor thesis [22]. Thus, the 480 nm wavelength is particularly important for accessing specific Rydberg states in ^{87}Rb in our own experimental setup. Due to the tunability of the laser, the experiment can probe a wide range of Rydberg states, opening up opportunities to study the interactions between Rydberg atoms and photons in the context of quantum nonlinear optics [11, 23].

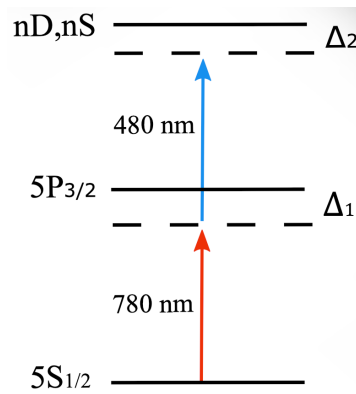


Figure 2.2: The ladder scheme of ^{87}Rb adapted from [24]. The excitation from the ground state ($5S_{1/2}$) to the intermediate state ($5P_{3/2}$) is done with the 780 nm probe laser. Afterwards the Rydberg excitation is done with a 480 nm control laser.

Frequency stabilization with the Pound-Drever-Hall (PDH) Method

As demonstrated in the previous chapter, very precise laser frequencies are vital for the transition of the rubidium atoms into Rydberg states. In this chapter, I will explain how the TASHGpro2 system was frequency stabilized with the help of an external reference cavity and the PDH method [25]. This will enable a stabilization in the sub-Hertz regime by locking the laser frequency to a high-finesse cavity, which will minimize frequency drifts caused by e.g. temperature fluctuations.

The PDH method essentially uses phase modulation, reflection measurements from the cavity and relies on a good feedback control system to keep the laser at resonance with the cavity. First, I will talk about the PDH method itself, with in-depth theoretical background in section 3.1. Afterwards, I will show the experimental setup I have built in section 3.3 and then I will demonstrate the different steps in order to locking the laser while presenting my results in section 3.3.

3.1 The PDH method

The Pound-Drever-Hall (PDH) technique is a widely used method to lock a laser frequency to an optical cavity [26]. Its principle can be broken down into the following steps:

1. Phase modulation of the laser field (in this case with an electro-optic modulator) to create sidebands.
2. Measuring of the reflection field or intensity from the cavity with a photodiode.
3. Extracting the error signal from the reflection, which indicates to which side the laser frequency is drifting with respect to the cavity resonance.
4. Using a feedback loop with the right parameters to correct the laser frequency and maintain stability on resonance.

In order to stabilize the frequency of the laser, the reference itself must be stable. Hence, an ultra-stable high-finesse Fabry–Perot resonator is chosen. The cavity consists of two mirrors with reflective surfaces facing each other. The resonance condition for monochromatic light is the following:

$$2L = n \cdot \lambda \quad (3.1)$$

where L describes the length of the cavity, n is an integer and λ the wavelength of the light [27]. Now, the distance between two modes, referred to as free spectral range (FSR), can be written as

$$\Delta\nu_{\text{FSR}} = \frac{c}{2L}, \quad (3.2)$$

when the relation $c = \lambda \cdot \nu$ for the speed of light c is used. The Finesse is described as the ration of the FSR to the full-width-half-maximum (FWHM) linewidth of the peaks

$$F = \frac{\nu_{\text{FSR}}}{\delta\nu_{\text{FWHM}}} = \frac{\pi\sqrt{r_1 r_2}}{1 - r_1 r_2}, \quad (3.3)$$

with r_1 and r_2 being the reflection coefficients of the two mirrors [27]. Therefore, a higher reflectivity accounts to a higher Finesse, which is necessary for achieving the needed results.

When light interacts with a surface, one needs to consider the transmitted and reflected part of the electric field. Now there are two cases to distinguish. In the first case, when the cavity is on resonance, the field performing round trips inside the cavity interferes constructively, and the reflected field and the leakage field of the first mirror undergo destructive interference. In the second case the transmission decreases and the reflection coefficient is non-zero. The leakage beam and the promptly reflected beam are not exactly 180° out of phase, and a complete destructive interference will not occur. However, the phase of the reflected light will indicate on which side of the resonance the laser is on [26]. In figure 3.1 the reflection coefficient and the phase shift are plotted. One can see, that the reflection coefficient becomes zero on resonance and that a phase shift occurs on the different sides of the resonances. The reflection transfer function R can be written as

$$\frac{E_r(\nu)}{E_{\text{inc}}(\nu)} \equiv R = r \left[\frac{1 - \exp(i\phi)(r^2 + t^2)}{1 - \exp(i\phi)r^2} \right], \quad (3.4)$$

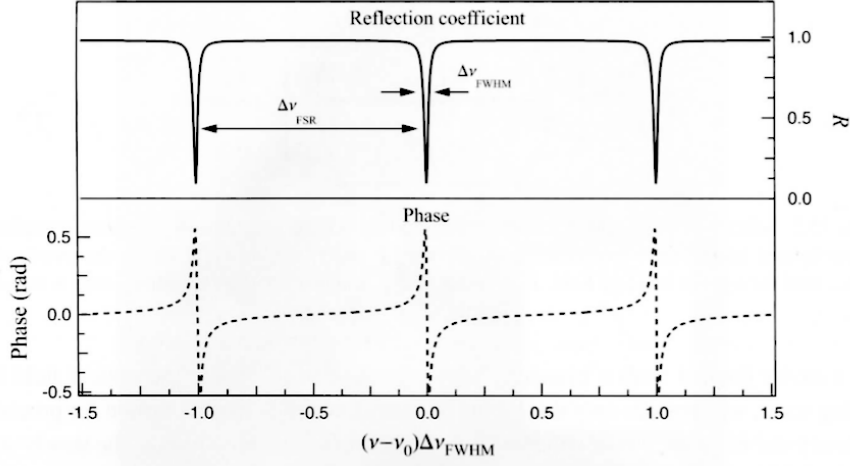


Figure 3.1: At the top one can see the reflection signal of the light with the resonance dips being spaced out in $\Delta\nu_{\text{FSR}}$ and the width is given by $\Delta\nu_{\text{FWHM}}$. The respective phase signal can be seen at the bottom which has a zero-crossing at resonance and a steep slope around resonance [28].

with the reflected and incident field $E_{r/\text{inc}}$ and transmission/reflection coefficients t/r and phase ϕ [28].

Knowing this, one can try to stabilize the frequency of the laser with a frequency modulation. The modulation will create sidebands which will not be on the same frequency as the incident and reflected field but in a definite phase relation to those. By interfering the sidebands with the reflected beam, a beat pattern will be shown and the phase of this exact pattern can be measured. This will allow us to determine the phase of the reflected beam [26, 28].

Electro-optic modulators (EOMs) are the driving force in this aspect, as they introduce phase modulation to create sidebands for locking the laser's frequency to an optical cavity. A polarization maintaining (PM) fiber is used to couple the light into and out of the setup. The integrated optical phase modulator from Jenoptik (PM980) is based on a Lithium niobate (LiNbO_3) crystal [29]. The fundamental principle behind EOMs is the Pockels effect, a linear electro-optic (EO) effect, where an applied electric field changes the refractive index of a non-centrosymmetric material, thereby altering the phase of light passing through it. For different polarization of the incoming light the refractive index is also different because they do not pass the material with the same velocity. In this case, the refractive index in the x- and y-axis is equal and is called the ordinary index n_0 , whereas the refractive index along the z-axis is called the extraordinary index n_e . The change of the effective refractive index Δn_{eff} is proportional to the applied electric field. Thus, the phase difference $\Delta\Phi$ can be written as

$$\Delta\Phi = \frac{2\pi}{\lambda} \Delta n_{\text{eff}} L \quad (3.5)$$

and the modulation efficiency is given by the half-wave voltage-length product

$$V_{\pi} L = \frac{d\lambda}{n_{\text{eff}}^3 r \Gamma}, \quad (3.6)$$

where r describes the effective EO coefficient and Γ the overlapping factor between the electric field and

the optical mode in the waveguide and L the length of the phase shifter [30].

LiNbO_3 is a widely used material for Pockels effect-based modulators because it offers a few advantages. They can operate across a wide range of frequencies and possess ultra-fast response times, making them versatile for applications from telecommunications to quantum optics. In addition, LiNbO_3 has been used for a long time and therefore offers great stability, commercial availability and engineerability for more efficient and tailorable work [31, 32]. However, in comparison to other ferroelectric-material-based devices it has a low EO coefficient and thus requires specific waveguides to lower the voltage-length product $V_\pi L$ [30].

For the modulation frequency, a small radio frequency synthesizer (SynthUSB) from Windfreak Technologies is used with a frequency of 555 MHz [33]. After the modulation of the phase the incident electric field can be describes as

$$E_{\text{inc}} = E_0 \exp[i(\omega t + \beta \sin \Omega t)] \quad (3.7)$$

and using the Bessel functions transformation, one can find

$$E_{\text{inc}} \approx [J_0(\beta) + 2iJ_1(\beta) \sin \Omega t] \exp(i\omega t) \quad (3.8)$$

$$= E_0 [J_0(\beta) \exp(i\omega t) + J_1(\beta) \exp[i(\omega + \Omega)t] - J_1(\beta) \exp[i(\omega - \Omega)t]] [26]. \quad (3.9)$$

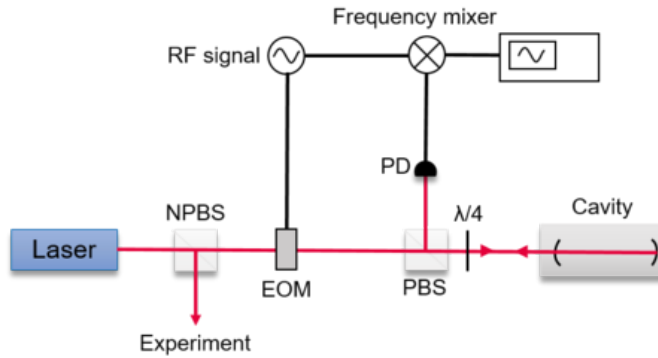
One can see, that the incident beam actually consists of three beam, namely the carrier with angular frequency ω and the two sidebands with frequencies $\omega \pm \Omega$ with the phase modulation frequency Ω and β is the modulation depth. Because we are interested in the reflection, as this will generate the error signal, and the power will be measured with a photodiode, we can simply multiply the terms with the reflection coefficient and calculate the square of the absolute value. In the end, the reflected power becomes

$$\begin{aligned} P_{\text{ref}} = & P_c |F(\omega)|^2 + P_s [|F(\omega + \Omega)|^2 + |F(\omega - \Omega)|^2] \\ & + 2\sqrt{P_c P_s} [\text{Re}[F(\omega)F^*(\omega + \Omega) - F^*(\omega)F(\omega - \Omega)] \cos \Omega t \\ & + \text{Im}[F(\omega)F^*(\omega + \Omega) - F^*(\omega)F(\omega - \Omega)] \sin \Omega t] \\ & + (2\Omega \text{ terms}), \end{aligned} \quad (3.10)$$

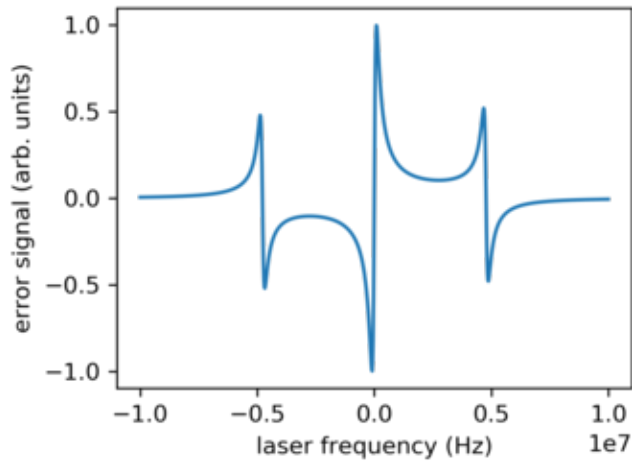
with P_c being the power in the carrier and P_s being the power in the sidebands. The resulting wave propagates with a nominal frequency of ω and the envelope consists of a beat pattern with two frequencies. There are also some interference terms from the carrier and sidebands (Ω) and from the sidebands to each other (2Ω) [26]. As only certain terms are relevant for the error signal, mainly the $\sin \Omega t$ and $\cos \Omega t$ term, these are isolated and guided into a mixer together with the reference radio frequency (rf) signal of the same frequency. Then, a DC signal proportional to the phase of the photodiode signal can be extracted [34]. Typically the error signal derived from a possible setup shown in figure 3.2(a) looks like the one shown in figure 3.2(b). Furthermore, for fast modulations near resonance the error signal is expressed as

$$\epsilon = -2\sqrt{P_c P_s} \text{Im} [F(\omega)F^*(\omega + \Omega) - F^*(\omega)F(\omega - \Omega)] , \quad (3.11)$$

as the sidebands are totally reflected and the carrier is near resonance consequently the cosine term in Eq. 3.11 can be neglected [26]. After the error signal, which is a function of the laser's frequency deviation, has been effectively generated, this top-of fringe principle can be used to lock the laser to the top of the



(a) Schematic setup for the Pound-Drever-Hall technique. Optical paths are depicted in red, electronic signal paths in black [34]. Once the light hits the non-polarizing beamsplitter (NPBS), the reflection can be used for an experiment and the transmission is used for the PDH method. The EOM creates an rf signal which is mixed with the PD reflection signal of the PBS in front of the cavity, which will create the error signal seen in 3.2. The transmitted beam is guided to the cavity.



(b) PDH error signal. It features a steep slope around the lock point at 0 Hz and a large capture range determined by the modulation frequency of 5 MHz. The second and third zero crossing at -5 and +5 MHz correspond to one sideband being resonant with the cavity and interfering with the reflected carrier and other sideband [34].

Figure 3.2: Overview of a possible setup and the error signal generated from the PDH method.

peak. For that implementation, it is also helpful to make use of the linear behavior of the error signal near resonance. As long as the frequency deviation $\delta\omega$ from the resonance is smaller than the cavity linewidth $\delta\nu = \Delta\nu_{\text{FSR}}/F$ the error signal is described as

$$\epsilon \approx -\frac{4}{\pi} \sqrt{P_c P_s} \frac{\delta\omega}{\delta\nu} \quad (3.12)$$

$$\epsilon = D\delta f, \quad (3.13)$$

making use of the relation $f = \frac{\omega}{2\pi}$ and defining the proportional constant as $D \equiv -\frac{8\sqrt{P_c P_s}}{\delta\nu}$ [26]. Finally, for the best signal-to-noise ratio, a feedback loop is integrated and with a controller the parameters for optimizing the lock can be chosen.

3.2 Feedback-loop and PID controller

Because we want the laser to be stabilized to a certain frequency and disturbances must be taken into account, a feedback loop makes sure that abrupt deviations are counteracted to preserve the set point. Additionally, the linewidth is also reduced as it is limited by noise which can be compensated in the lock. In a closed-loop control system, the current value is compared to the desired set point and the difference, derived from the error signal, is given as feedback and corrected through a controller [35, 36]. A block diagram of a closed loop control is shown in figure 3.3.

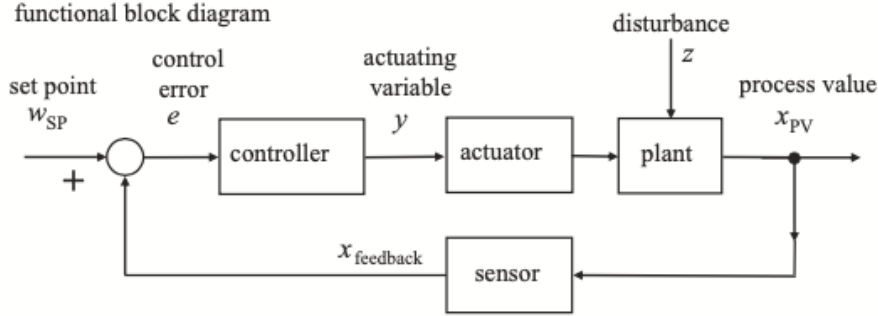


Figure 3.3: Functional block diagram of a closed loop control [36]. Here, the set point w_{SP} is used as reference. Any difference will be given as control error e to the controller, which then gives a command y to the actuator. Outer disturbances z , like noise, is also taken into account. Through a sensor a feedback $x_{feedback}$ is given and compared to the the current processes value x_{PV} and its deviation from the set point.

The system analysis can be done with different method. Even though the time domain will allow to describe the dynamic behavior of the system with physical laws, it is much simpler to analyze the system in the Laplace-Domain as the complex differential equations can be easily solved. This is done with the help of the Laplace-transformation

$$f(s) = \int_{-\infty}^{\infty} f(t)e^{-st} dt, \quad (3.14)$$

in which s is called the Laplace-operator and $f(t)$ is a continuous function with the time t as argument. A transformation of the real time-domain to the frequency domain is made but in contrast to the Fourier-transformation it can be applied to more functions as the parameter s is expanded to the complex dimension. Therefore, transfer functions can be derived, which describe the relation between an input and output of the system without having to back transform into the time domain as this will be too complicated [35, 36]. Then the relation

$$Y(s) = T(s)R(s) + S(s)D(s) \quad (3.15)$$

between the transformed output $Y(s)$, the reference or set point $R(s)$ and the noise $D(s)$ can be established with the reference transfer functions $T(s) = \frac{P(s)C(s)}{1+P(s)C(s)F(s)}$ and the disturbance transfer function $S(s) = \frac{1}{1+P(s)C(s)F(s)}$. $C(s)$ describes the transfer function of the controller and $P(s)$ the plant or actuator whereas $F(s)$ describe the sensor [37]. Eq. 3.15 gives insight on what requirements must be taken into account for choosing the controller. The first condition is that the overall phase of the term $P(s)C(s)F(s)$ should not reach 180° as this will start to amplify the deviation from the set point and

ruin its purpose, hence the phase delay should have a value between -90° and 90° . The second condition dictates that for values of frequency s smaller than the loop bandwidth s_{bw} the gain of the feedback loop should be larger than 1 and smaller for s larger than s_{bw} [37].

Proportional-Integral-Derivative (PID) controllers are widely used because they offer a stable and robust performance over a wide range of operating conditions. The contribution to the control signal is a sum of a proportional, integral and derivative part proportional to the error signal [35, 37]. Therefore the control signal and its transfer function can be described by the following formulas:

$$u(t) = K_p \cdot e(t) + K_I \int_0^t d\tau e(\tau) + K_D \cdot \frac{de(t)}{dt} \quad (3.16)$$

$$C(s) = K_p + \frac{K_I}{s} + K_D s \quad (3.17)$$

Thus, each term has different advantages since the K_I term is most effective for lower frequencies and the K_D term gains importance in the higher frequency domain while the K_p term acts intermediately [37]. Additionally, a phase shift of -90° is imposed in the integral term and a shift of 90° in the derivative term.

For this laser, the FALC pro controller from TOPTICA was combined with the DLC pro, allowing for an optimal and smoother choice of feedback parameters. It offers a Bandwidth of 50 MHz with a signal delay of 10 ns.

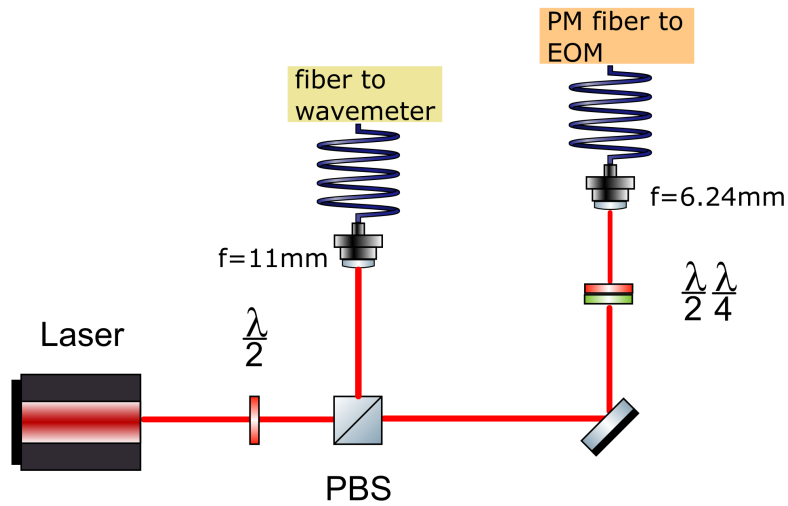
3.3 Setup and results

After the theoretical foundations have been laid out, I will describe the setup I have built for the TASHGpro2 laser system. The setup in front of the laser is shown in figure 3.4. With the help of a $\lambda/2$ waveplate the polarization axis of the beam is adjusted and split into two directions with the polarizing beamsplitter. As mentioned in the previous section 3, the polarization alignment of the incoming light is important for the EOM. The cube splits the s- and p-polarization components, because of its different coatings and the s component is reflected while the p component passes through [38]. Therefore, the reflection is coupled into a fiber which is connected to a wavemeter and the transmission is coupled into the EOM fiber after being guided to a quarter and half plate to guarantee the polarization alignment to the fast/slow axis of the polarization maintaining fiber. It is also important to match the key of the fiber adapter with the polarization of the light, which is in this case in the horizontal layer (or parallel to the optical table). With the wavemeter the current frequency of the laser can be measured.

Then, the light from the EOM fiber can now be out coupled and collimated at the other side of the optical table where the external reference cavity was placed. The setup for locking the laser to the cavity is shown in figure 3.5. First, the light hits a polarizing beamsplitter and the reflected beam is neglected. The transmission is guided through three mirrors towards another polarizing beamsplitter, where also the other laser emissions from the experiment pass through, and enters the cavity. Because of a dichroic mirror in front of the cavity and different polarization of the laser beams, they can be locked to the cavity without disturbing one another. If the light is not fully transmitted inside the cavity and some part of it is reflected, it can be measured with the photodiode in reflection of the first beamsplitter after the fiber optics.

In order to get the best efficiency, a coupling to the ground mode is desired. The ground mode has the same Gaussian profile as the incoming beam, which leads to the biggest error signal. But apart from the longitudinal modes (see eq. 3.1 and 3.2) high-order transverse modes will also be excited, because in reality a perfect coupling cannot be guaranteed. The resonance frequencies of these modes are different from the fundamental mode. Therefore, a suppression of high-order modes is vital. The transverse mode structure of the light inside the cavity can be viewed with a camera in transmission and used as help when trying to adjust the mirrors. In figure 3.6 the different modes, captured with the camera, are visible. The first figure 3.6(a) shows the appearance of high-order modes, when the coupling is not efficiently done. After adjusting the coupling, the ground mode (fig. 3.6(b)) is visible. With the help of the oscilloscope *PicoScope*, the transmission could be measured for the ground mode and high-order modes, which still appear but are greatly suppressed (fig. 3.7) The transmission without the modulation of sidebands can be seen in figure 3.7(a) and in figure 3.7(b) the modulation was created with the amplified output of a DDS *windfreak SynthUSBII2019* with a frequency of 555 MHz. A photodiode was used in transmission for the optimal coupling to the ground mode and the suppression of high-order modes. For a maximal scan amplitude of 2.466534 V peak to peak, offset of 84.996 V and scan frequency of 4 Hz, the ground mode has an average of 1 V and the high order modes were 27 mV. Thus, the high order modes are greatly suppressed to about 3% of the ground mode. This is enough for a stable lock as all high-order modes close to the ground mode are suppressed even further and not visible.

The next step is setting up the FALC module to create the feedback loop. It is a digitally controlled fast laser locking module and has a PI^3D^2 regulator and is used in combination with the PDH module and the DLC pro, where the reflection signal is fed into [39]. From the PDH module a modulation of 25 MHz is given to the EOM and from the error/local oscillator channel a signal is given to the non-inverting channel of the FALC module. Then, from the FALC module, the slow branch is established with connecting

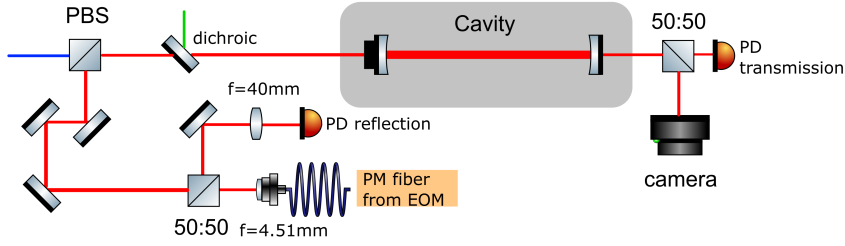


(a) Sketch of the setup.

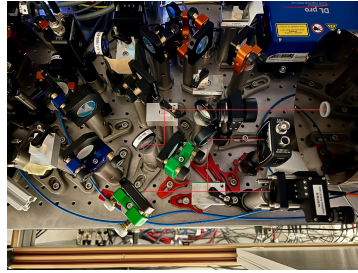


(b) Photo of the setup.

Figure 3.4: Setup after the 960 nm beam exits the laser system. First, the light passes through a half waveplate to ensure correct polarization before its hits a polarizing beamsplitter. The s component is reflected and couples into a fiber which is connected to a wavemeter. The p component is transmitted to the EOM fiber. In front of the EOM fiber an alignment of a half and quarter waveplate further guarantee correct polarization for the EOM fiber.



(a) Sketch of the setup.



(b) Photo of the setup.

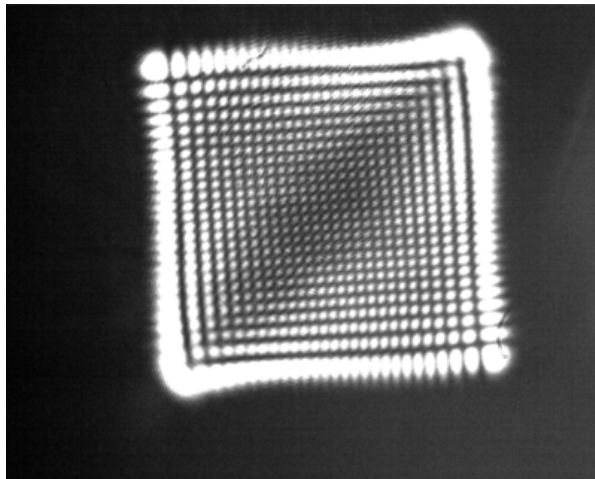
Figure 3.5: Setup in front of the cavity. The beam passes through a polarizing beamsplitter and the transmission is guided by mirrors towards another PBS, where it is reflected to the cavity. The reflection from the cavity is going back until it hits the first PBS again and the power is detected with a photodiode, where the error signal can be extracted. The transmission of the cavity can also be measured with a PD after the cavity and the transverse modes can be viewed with a camera.

the unlimited channel to the MC+ module of the DLC pro and in the fast branch the main channel is connected to the DC mod channel of the laser. Hence, the fast circuit immediately controls the current of the laser, whereas the slow circuit aims for canceling out long term instabilities by acting on the grating piezo of the laser. Now, the laser can be locked and different parameters of the PID-controller can be tested out to optimize the lock. The error signal from the photodiode was measured and plotted in figure 3.8 and is has the typical shape of the error signal mentioned in section 3.1.

Additionally, the FALC monitor channel was connected to a spectrum analyzer to look at the frequency behavior and noise characteristics. The FALC extension on the TOPTICA software also offers the creation of the theoretical gain and phase curves of the PID as functions of the frequency, so called bode plots, which has proven to be very useful.

Bode plots show the behavior of the gain and the phase in dependence of the frequency and therefore offer a good way to see the effects of the chosen parameters for the feedback. The magnitude plot is additionally in logarithmic scale and multiplied with the factor 20, i.e. in units of decibel (dB) [36]. As mentioned in section 3.1, a phase shift of 180° has to be avoided and a too large proportional gain might cause oscillations rather than stabilizing the system. The Integral gain is more precise, but does not act immediately like the proportional gain. Also, a phase shift of -90° is caused and because it integrates the difference from the set point the response to the system might overshoot. The derivative gain is used in combination with a P and I gain and only acts on the change of velocity. Combining these three parameters will give the most effective controller for the feedback.

The bandwidth of the feedback also plays a crucial role since a stable and robust lock is desired by



(a) High-order modes



(b) Ground mode

Figure 3.6: Transverse modes in the cavity viewed with a camera in transmission.



(a) Transmission (Channel E) and Trigger (Channel C). The highest peaks resemble the ground-mode.



(b) Now windfreak is turned on for the modulation of sidebands.

Figure 3.7: Transmission of the cavity measures with a photodiode (a) without and (b) with windfreak. In the first case one can see the transmission peaks of the ground-mode, whereas the high-order modes are barely visible. In the second case the sidebands are created with windfreak causing a lower power of the ground mode and additional resonances.

minimizing noise. It is therefore desired to push the bandwidth towards higher frequencies. However, if a critical phase shift is reached, the feedback does not limit the noise but enhances it. This limit is called the servo bandwidth or servo bump [40, 41]. Typically, these noise bumps occur around few 100 kHz to a few MHz the latter being desired in the context of our experiments involving Rydberg atoms [42].

For different parameters of the PID displayed in table 3.1 the plots in figure 3.9 could be created. One can see, that in the last row, without the derivative terms, the servo bandwidth is way too low indicating a poor noise reduction and ineffective feedback. In the first row the servo bandwidth is in a good region as it has a value of roughly 1.6 MHz. In the second row the servo bandwidth is slightly lower and the "bump" resembles a peak or resonance, caused by the 180° phase shift and is therefore not desired. After doing an alternative noise characterization explained in section 4, different settings were made and the lock could be further improved. The parameters for the second measurement can be seen in Tab. 3.2 and the plots in figure 3.10. Unlike before, the servo bump is even further suppressed and still pushed to roughly 1.5 MHz. In conclusion, the method has proven to be very effective and the laser can be easily locked and offers a stable frequency for the desired use in the future.

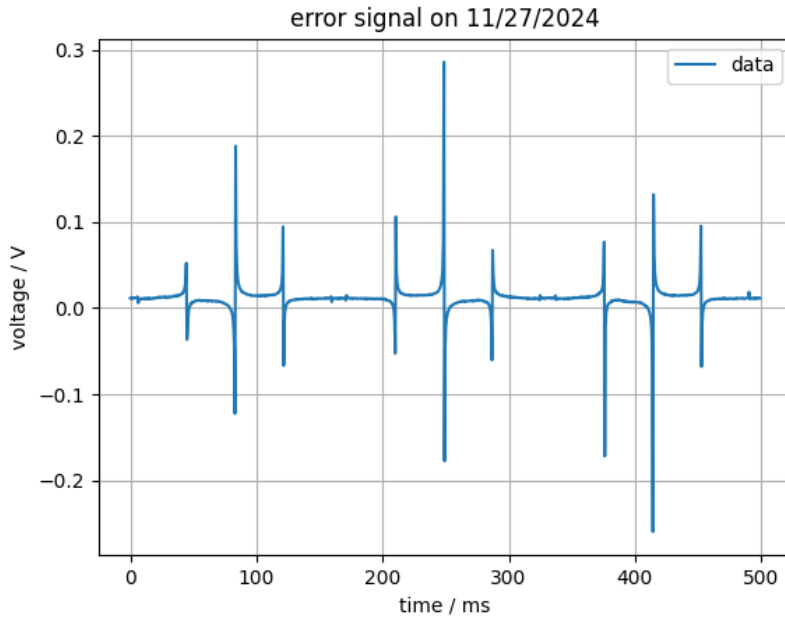


Figure 3.8: PDH Error signal measured while scanning the laser on the 11/27/2024. One can see the steep slopes at the lock points, i.e. at resonance and the two crossings at the sides of the steep slope. These are the zero crossings caused by the resonances of the sidebands.

Table 3.1: Settings for the different parameters in the plots of figure 3.9

Number	G / dB	I ₁ / kHz	I ₂ / Hz	D ₁ / kHz	D ₂ / kHz
1	-18.5	15	470	190	700
2	-16.5	15	470	190	100
3	-21.5	31	220	0	0

Table 3.2: Settings for the different parameters in the plots of figure 3.10

Number	G / dB	I ₁ / kHz	I ₂ / Hz	D ₁ / kHz	D ₂ / kHz
1	-21.5	15	470	190	700
2	-23.5	15	470	190	700
3	-21.5	15	470	400	700

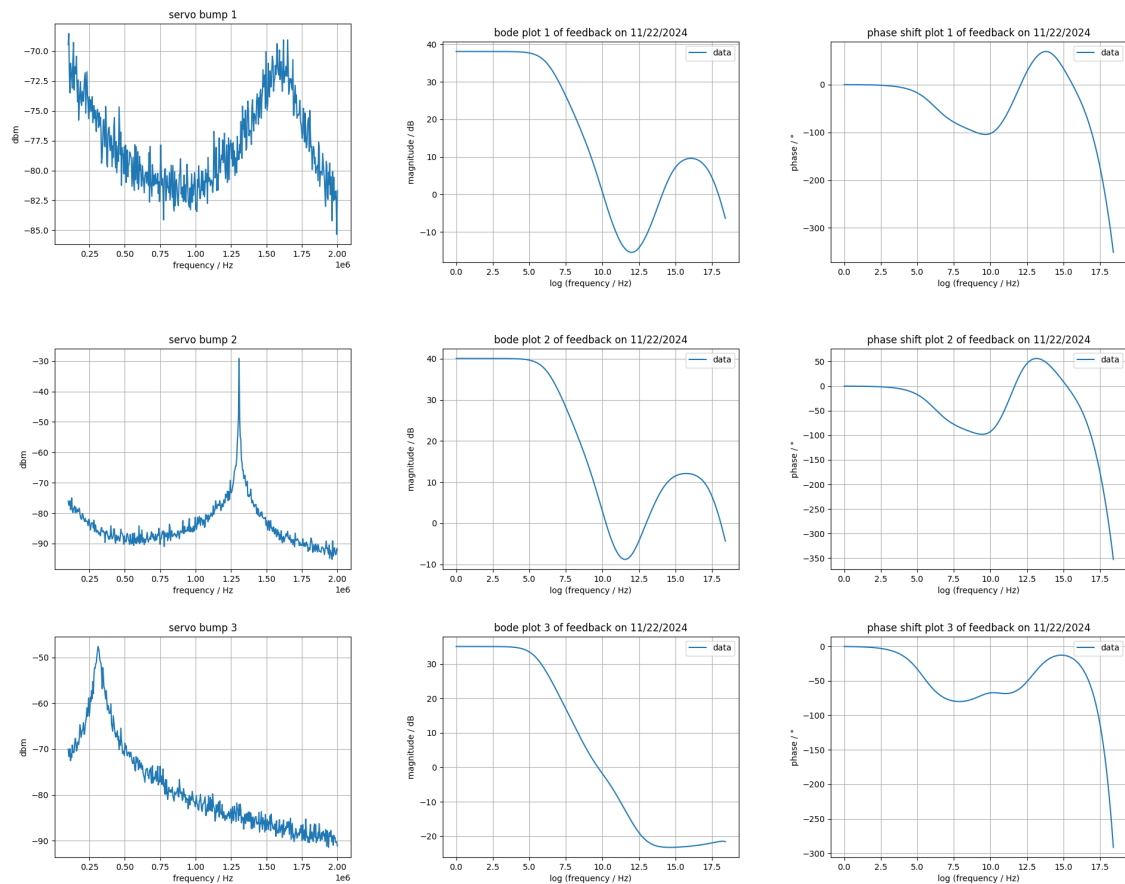


Figure 3.9: Measurements taken with the spectrum analyzer for different control parameters (Tab. 3.1) and the corresponding bode plots and phase shift plots. The servo bump as well as the bode plots and phase shift plots have different characteristics depending on the chosen parameters.

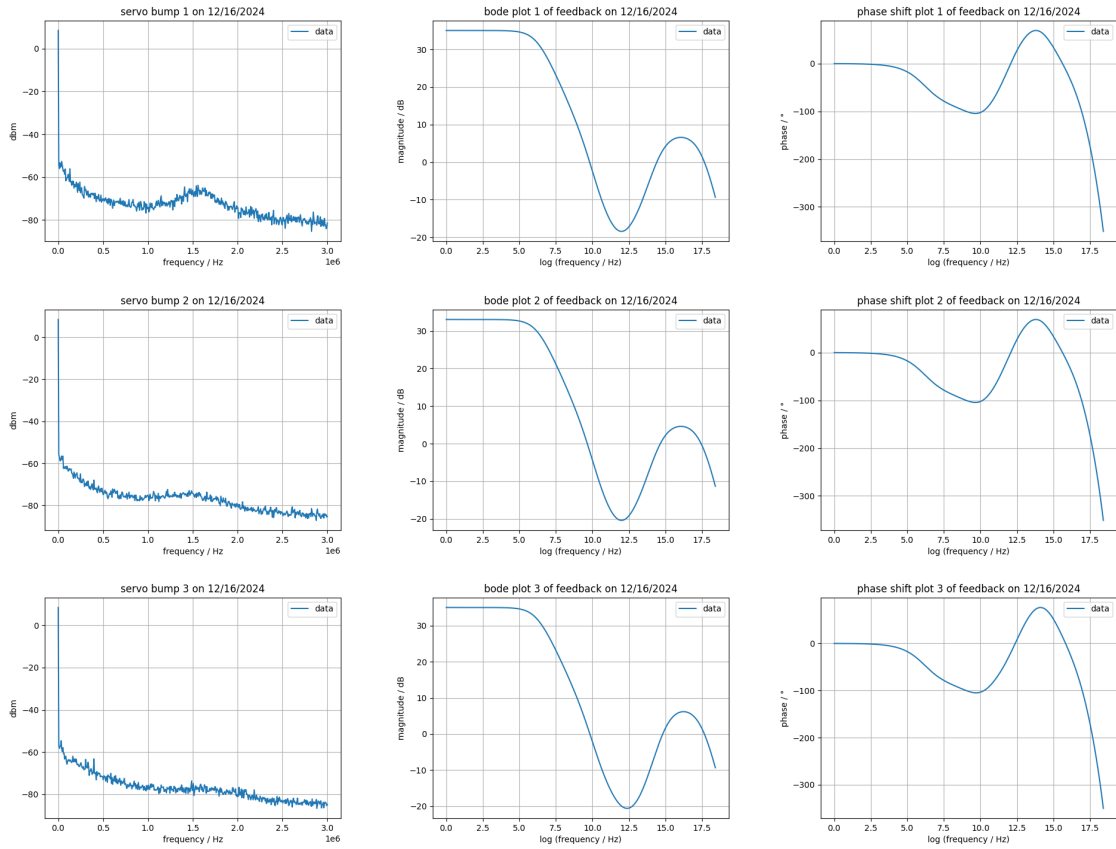


Figure 3.10: Second measurements taken with the spectrum analyzer for different control parameters (Tab. 3.2) and the corresponding bode plots and phase shift plots. The servo bump as well as the bode plots and phase shift plots have different characteristics depending on the chosen parameters.

Noise characterization with a Mach-Zehnder-Interferometer

A Mach-Zehnder-Interferometer (MZI) is a versatile tool in precision optics, enabling detailed analysis of laser coherence and noise characteristics. In this thesis, the MZI was employed to perform noise characterization of the stabilized laser system using a Lecroy oscilloscope and a network analyzer. This characterization focused on quantifying residual frequency noise, phase noise, and laser linewidth after the previously gained knowledge and results of the stabilization with the PDH method. The results of the noise characterization could be used to compare and improve the lock settings. As the MZI was set up by Simon Schroers and will be topic of his master thesis, I will only briefly talk about the theoretical background in section [4.1](#) and discuss the setup and results in [4.2](#).

4.1 Theoretical background

Interferometers have different kinds of uses like distance determination in metrology, refractive-index measurement or spectrometry [43]. An Interferometer creates a superposition of electromagnetic waves, after the incident light has been split in two optical paths. In addition, the changes in the optical path result in a variation of the intensity pattern of the detected light, depending on the phase difference of the two beams [44].

If the condition $n \cdot \lambda = \Delta L$ is fulfilled, it corresponds to constructive points in the pattern, whereas the condition $(n + \frac{1}{2}) \cdot \lambda = \Delta L$ corresponds to destructive points. The Intensity of the overlapping beams is written as

$$\begin{aligned} I &= |E_1 + E_2|^2 \\ &= E_1^2 + E_2^2 + 2E_1E_2 \cos(\Delta\phi) \end{aligned}$$

where I is the intensity, E the electric field and $\Delta\phi = \frac{2\pi nL}{\lambda}$ the phase difference [45, 46]. Hence, the latter is also called the interference term.

The measured phase noise can be translated to a frequency noise in order to determine the stability of the laser. This relationship is defined as

$$S_v(f) = f^2 S_\phi(f) \quad (4.1)$$

where $S_\phi(f)$ is the phase noise power spectral density (PSD), $S_v(f)$ the frequency PSD and f the Fourier frequency [47]. As the lock point of the interferometer is chosen where the transmission signal, a \cos^2 function, shows a linear behavior, that is the slope, a small deviation or change in voltage can be translated to a change in phase. The frequency deviation $\Delta\phi$ can be written as a composition of different frequencies

$$\Delta\phi = 2\pi \int_t^{t+\tau} f(t') dt' \quad (4.2)$$

$$\Delta\phi = 2\pi \sum_t \sqrt{2S_v \Delta f} \int_t^{t+\tau} \cos(2\pi f_i t + \phi_f) dt' \quad (4.3)$$

where $f(t) = \sum_{f_i} \sqrt{2S_v \Delta f} \cos(2\pi f_i t + \phi_f)$ is the composition with random phase ϕ_f and delay time τ . This can be further simplified to:

$$\Delta\phi = \sum_{f_i} \sqrt{2S_v \Delta f} \frac{2 \sin(\pi f_i \tau)}{f_i} \cos(2\pi f_i t + \pi f_i \tau + \delta\phi_f)$$

The sin term is the suppression term that needs to be considered in the measurements. In the measurements the spectrum analyzer measures the frequency deviation as $\Delta f(t) = \sum_{f_i} \sqrt{2S_v' \Delta f} \cos(2\pi f_i t + \delta\phi_f)$. But in reality it behaves like the following:

$$\Delta f(t) = \frac{\Delta\phi}{\tau \cdot 2\pi} = \frac{1}{\tau \cdot 2\pi} \sum_{f_i} \sqrt{2S_v \Delta f} \frac{2 \sin(\pi f_i \tau)}{f_i} \cos(2\pi f_i t + \pi f_i \tau + \delta\phi_f). \quad (4.4)$$

Therefore the transformation

$$S_{v,i}\Delta f = \left(\frac{f_i \cdot \tau \cdot \pi}{\sin(\pi f_i \tau)}\right)^2 \cdot S'_{v,i} \quad (4.5)$$

must be taken into account. The spectral density has a unit of Hz^2/Hz . The formulas were derived by Simon and will be discussed in detail in his master thesis.

4.2 Setup and results

The setup of the is shown in 4.1. First, the laser light is coupled out the fiber and passes through a half waveplate before it hits the PBS. Thus, two optical paths are created. In the upper path, the reflected path, the beam is again reflected through a mirror and hits the BS and is guided to the photodiode. For the transmitted beam the optical path is delayed with a fiber and afterwards the beam is reflected with a piezo mirror and also hits the BS where an interference with the other beam takes place. The half waveplates along the way have to be adjusted to the wavelength of the analyzed laser. If the photodiode does not measure anything or the signal drifts away from the slope, a feedback with a PID controller corrects the position of the piezo mirror.

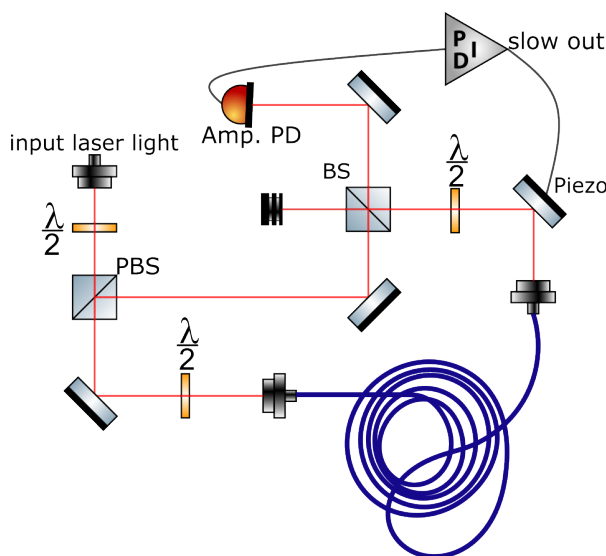
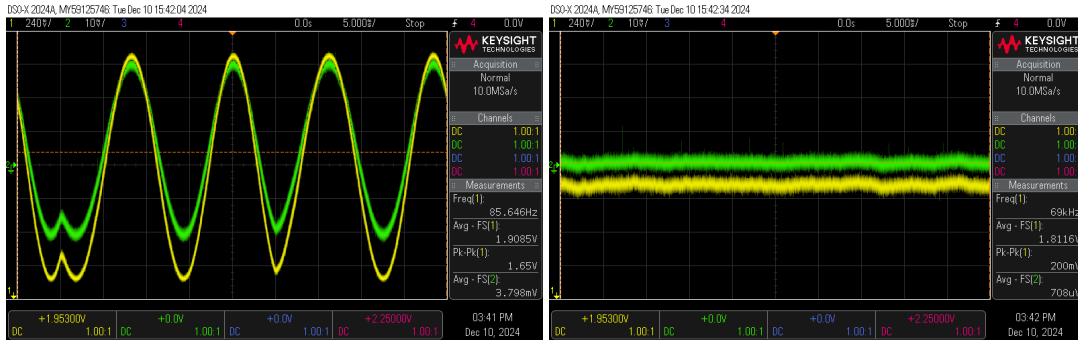


Figure 4.1: Setup of the MZI. The input light is split into two optical arms by an PBS and one arm is delayed with an fiber. Afterwards they come together on the BS and hit a PD, where the interference signal is detected. The PD also gives feedback with a PID controller to the piezo mirror in the delayed arm in case of drifts.

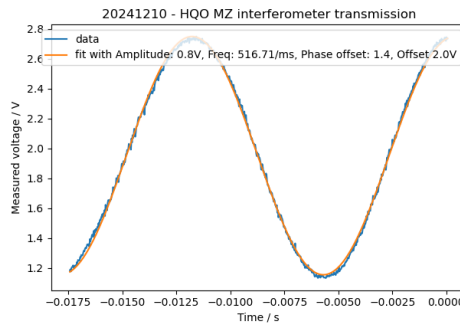
After adjusting the fiber optics and the position of the mirrors, an interference signal could be seen on the oscilloscope (fig 4.2). As expected, the signal in figure 4.2(a) shows a \cos^2 function while scanning. Now, the slope of the function is used as lock point. Therefore the locked signal in figure 4.2(b) should be symmetrical around zero. Due to insufficient protection from disturbances such as vibrations or temperature, the whole setup is very fragile and sensitive. Therefore the signal must be closely monitored while taking measurements, as the signal potentially drifts too far away from zero that not even the PID controller can efficiently take countermeasures.

If the signal is stable, measurements can be taken. First, the frequency nose was measured with a network analyzer. With a *GPIB Configurator* the parameters (linear/logarithmic, decades averages, termination) for the measurements could be send to the network analyzer. All the measurements were taken with a logarithmic scale, three decades, 10 averages and a termination of 1 M Ω (fig. 4.3). Three data sets were taken: the background, the unlocked laser and the locked laser. The PID settings are the same as the first one in Table 3.1. The raw spectrum is seen in fig. 4.3(a), in fig. 4.3(b) the background is subtracted and in 4.3(c) the y-scale is converted from dBm in the spectral density unit Hz²/Hz. In between the three decades there is a visible "cut", which is not coming from the data itself but is an



(a)

(b)



(c)

Figure 4.2: Signals of the PD visualized with an oscilloscope and terminated with $50\ \Omega$. The yellow signal corresponds to the PD signal and the green signal corresponds to the monitor signal of the lock box. (a) shows the transmission signal while scanning and (b) shows the signals locked to the slope of the transmission signal. In addition, a calibration of the transmission signal (c) was done.

internal problem of the network analyzer. As before in the first plot of fig. 3.9 the servo bump is above 1 MHz and another peak can be seen in the kHz regime. However, as the green data resembles the background and the peak is detected both in the unlocked case and especially big in the locked case, it seems that there is quite a disturbance but its origin is not clear as for now. Besides that, the frequency noise below the servo bandwidth is greatly suppressed.

Then, another measurement was taken with the LeCroy oscilloscope seen in figure 4.4. It has the advantage that the data can be Fourier transformed internally. In the first plot, one can see the three different data sets, which are then further processed by subtracting the data in the second plot and doing a correction in the third plot. The code was provided from Simon and involves some theoretical insight which will be described in detail in his thesis. The data is "noisy" in the high-frequency regime, which could come from the Welch power estimations made in the code that loses its effectiveness in the high-frequency domain. Also, there are some dips visible in the 10 MHz regime which could be corrected by including the suppression term. Again, the servo bump is visible in the 1 MHz range and the same peak seen in the network analyzer is also recorded with the LeCroy. Other than that the noise suppression works very well.

After improving the PID parameters for the feedback, another measurement was done with the network analyzer (fig. 4.5) and the LeCroy (fig. 4.6) with the parameters three of table 3.2. The servo bump

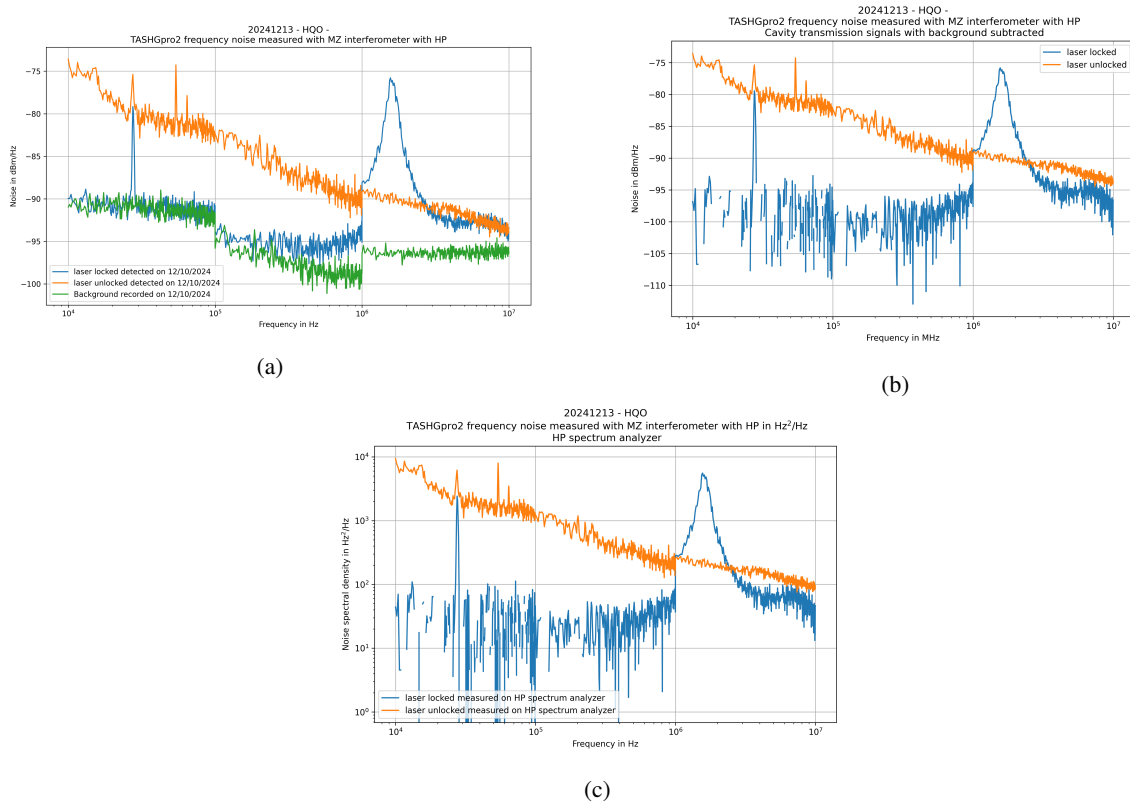


Figure 4.3: Frequency noise measured with the network analyzer. Parameters: 10 averages, 3 decades and 1 M Ω termination. The measurements were done with the first PID parameters in table 3.1. (a) Raw spectrum of the frequency noise. The green data is the background, the blue the locked case and orange the unlocked. (b) Frequency noise with the background subtracted. The blue data represents the locked data and orange the unlocked. (c) Frequency noise converted to Hz²/Hz.

could be reduced even further, indicating a better and stable lock. Because the peak in the kHz regime was quite noticeable I compared the data with some of the data of Simon. As seen in figure 4.7, a lot of peaks measured with the TASHGpro2 are also measured with lasers from another lab. This also includes the big peak in the kHz regime. Therefore it is very likely that something in the RQO lab or setup, maybe some cables or the piezo mirror, is the origin of these resonances. All in all, the noise characterization of the MZI has proven to be a very useful tool in improving the lock.

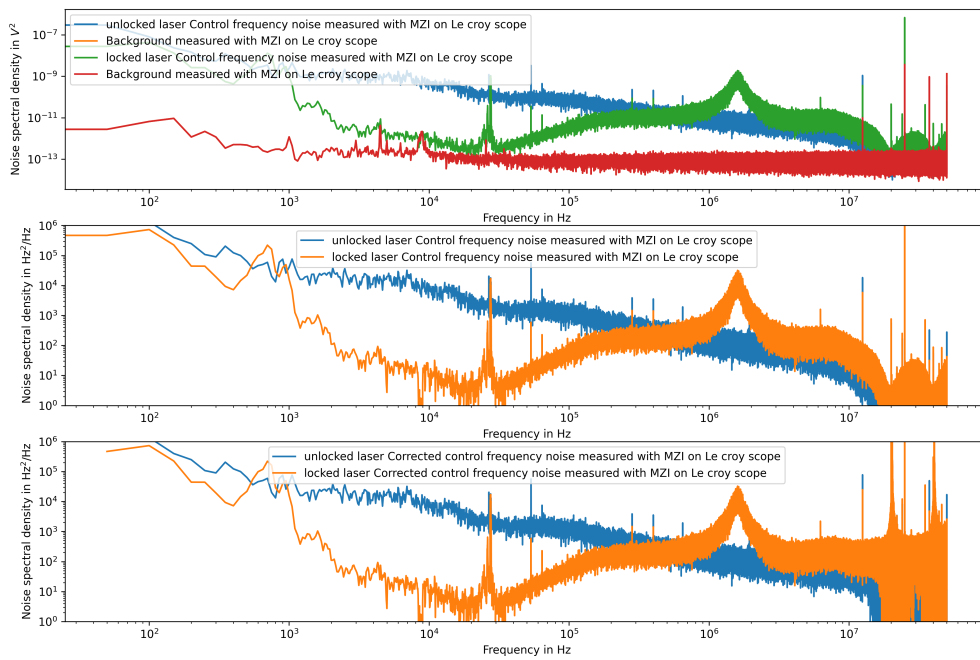


Figure 4.4: Frequency noise spectrum measured with the LeCroy. The first plot shows the background (red), the unlocked data (blue) and the locked data (green). In the second plot the background is subtracted and in the last plot some corrections were made to erase the dips in the high-frequency regime. The measurements were done with the first PID parameters in table 3.1.

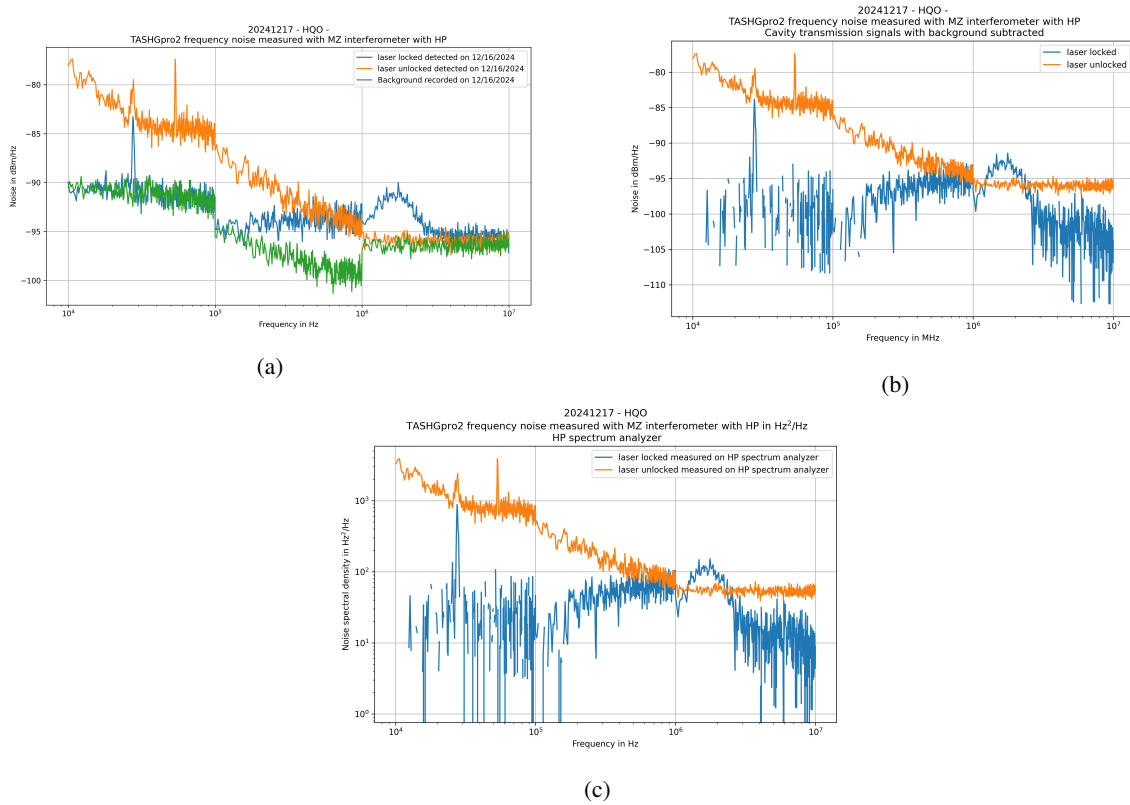


Figure 4.5: Frequency noise measured with the network analyzer. Parameters: 10 averages, 3 decades and $1\text{ M}\Omega$ termination. The measurements were done with the third PID parameters in table 3.2. (a) Raw spectrum of the frequency noise. The green data is the background, the blue the locked case and orange the unlocked. (b) Frequency noise with the background subtracted. The blue data represents the locked data and orange the unlocked. (c) Frequency noise converted to Hz^2/Hz .

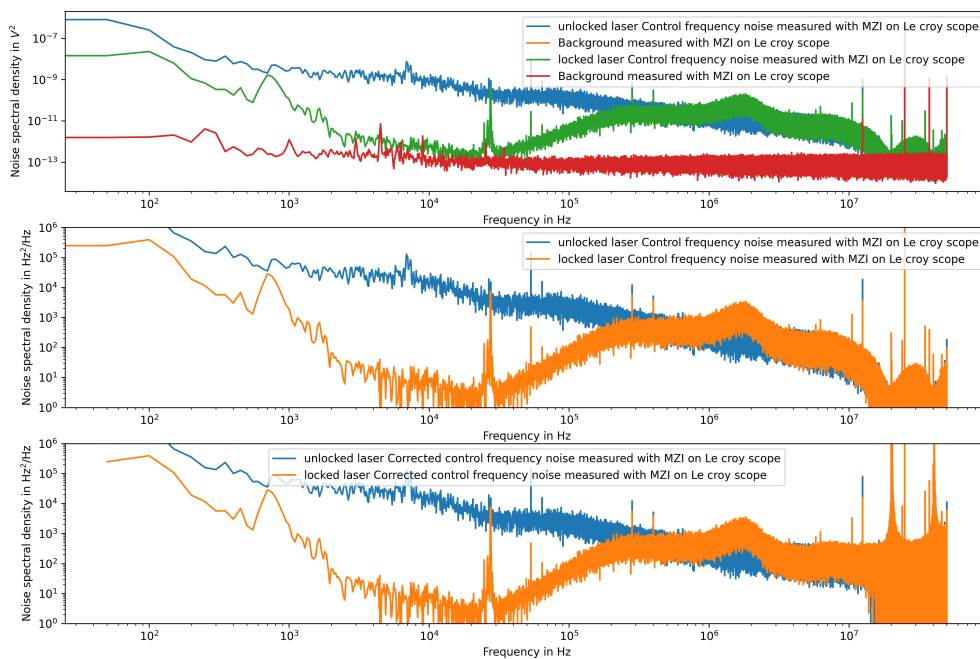


Figure 4.6: Frequency noise spectrum measured with the LeCroy. The first plot shows the background (red), the unlocked data (blue) and the locked data (green). In the second plot the background is subtracted and in the last plot some corrections were made to erase the dips in the high-frequency regime. The measurements were done with the third PID parameters in table 3.2.

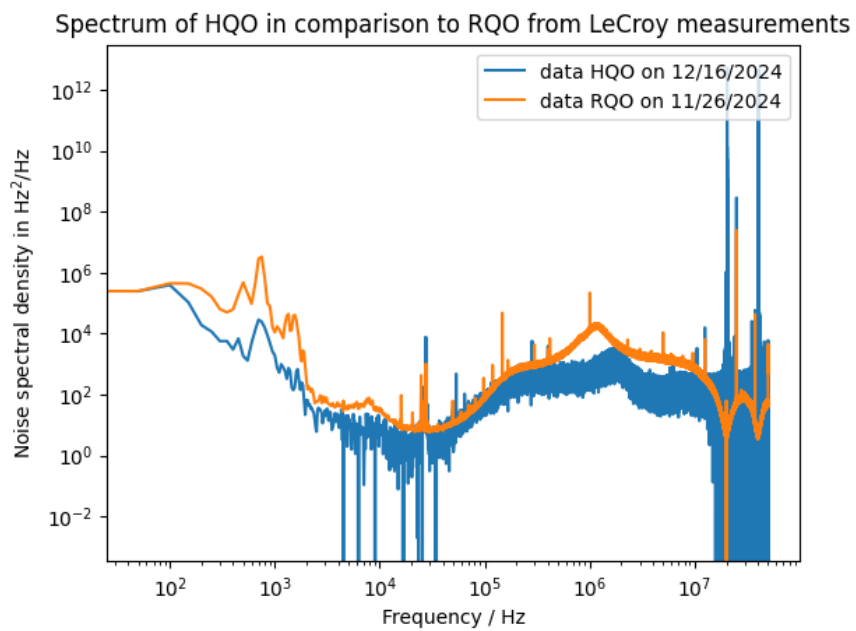


Figure 4.7: Comparison of the LeCroy measurements of RQO control laser and HQO TASHGpro2.

Conclusion and Outlook

This thesis focused on the setup and stabilization of a Rydberg excitation laser, with an emphasis on frequency stabilization to an ultra-stable reference cavity using the Pound-Drever-Hall method.

The first part of the thesis provided an overview of the theoretical foundations underlying the interaction of light with Rydberg atoms and the principle of nonlinear quantum optics. In addition, the relevance of ultra-stable lasers for precise photon-photon interactions was established, which is critical for enabling single-photon non-linearities and advancing hybrid quantum systems.

The second part detailed the characterization and optimization of the TASHGpro2 laser, focusing on its suitability for accessing Rydberg states in ^{87}Rb . Also, the implementation of the PDH method was discussed, from generating the error signal to designing a robust feedback loop with PID control. Experimental results demonstrated the stabilization of the laser including the push-back of the servo bump to about 1.5 MHz, highlighting the effectiveness of the stabilization technique.

Finally, noise characterization of the stabilized laser was performed using a Mach-Zehnder-Interferometer. This work provided insights into the residual noise sources and quantified the laser's performance in terms of power spectral density and frequency noise. These measurements validated the stabilization process while also identifying possible external noise contributions that could be analyzed further.

In the future the laser can be implemented in the experiment as control beam for the excitation to Rydberg states. Therefore, it might be interesting to see how long the laser is in lock and do some long-term measurements as these are also a current task at HQO.

Overall, the thesis successfully addressed the central objective of achieving a stable and precise laser source for future implementation in the experiments regarding Rydberg-mediated quantum optics and photonics.

Bibliography

- [1] S. Lyagushyn, ed., *Quantum Optics and Laser Experiments*, Print, Rijeka, Croatia: IntechOpen, 2012.
- [2] J. Garrison and R. Chiao, *Quantum Optics*, 2nd ed., Oxford University Press, 2008.
- [3] A. Allevi, S. Olivares, and M. Bondani, *Special Issue on Basics and Applications in Quantum Optics*, Applied Sciences **11** (2021) 10028.
- [4] Nonlinear Quantum Optics Group, University of Bonn, *Research Overview*, URL: <https://www.nqo.uni-bonn.de/research> (visited on 01/02/2025).
- [5] J. D. Pritchard, K. J. Weatherill, and C. S. Adams, “Non-linear optics using cold Rydberg atoms,” *Annual Review of Cold Atoms and Molecules*, World Scientific, 2013 301.
- [6] T. Peyronel, O. Firstenberg, Q. Y. Liang, et al., *Quantum nonlinear optics with single photons enabled by strongly interacting atoms*, Nature **488** (2012) 57.
- [7] Nonlinear Quantum Optics Group, University of Bonn, *Hybrid Quantum Optics*, URL: <https://www.nqo.uni-bonn.de/research/hybrid-quantum-optics> (visited on 01/02/2025).
- [8] J. Gamper, *Atom Preparation and Rydberg Excitation of Rubidium Atoms*, Master’s thesis: University of Bonn, 2024, URL: <https://www.nqo.uni-bonn.de/publications/publications/2024-julia-gamper-master.pdf>.
- [9] O. Firstenberg, C. S. Adams, and S. Hofferberth, *Nonlinear quantum optics mediated by Rydberg interactions*, Journal of Physics B: Atomic, Molecular and Optical Physics **49** (2016) 152003, Special Issue on Rydberg Atomic Physics, Published 30 June 2016.
- [10] R. W. Boyd, *Nonlinear Optics*, 3rd, Chantilly: Elsevier, 2008.
- [11] Y. O. Dudin and A. Kuzmich, *Strongly Interacting Rydberg Excitations of a Cold Atomic Gas*, Science **336** (2012) 887.
- [12] D. B. Tretyakov et al., *Two-Photon Laser Excitation of Rb Rydberg Atoms in the Magneto-Optical Trap and Vapor Cell*, Photonics **10** (2023) 1201.
- [13] Y. Wu, F. Qin, Y. Li, Z. Ding, and R. Xu, *Designing an Automatic Frequency Stabilization System for an External Cavity Diode Laser Using a Data Acquisition Card in the LabVIEW Platform*, Applied Sciences **14** (2024) 308.

Bibliography

- [14] TOPTICA Photonics AG, *TA-SHG pro: Tunable Frequency-Converted Diode Laser*, URL: <https://www.toptica.com/products/tunable-diode-lasers/frequency-converted-lasers/ta-shg-pro> (visited on 01/07/2025).
- [15] TOPTICA Photonics AG, *TA-SHG pro Resonator Image*, URL: https://www.toptica.com/fileadmin/_processed_/1/0/csm_toptica_TA_SHG_pro_resonator_7ef4ae03ab.jpg (visited on 01/07/2025).
- [16] L. A. Coldren, S. W. Corzine, and M. L. Masanovic, *Diode Lasers and Photonic Integrated Circuits*, Wiley, 2012.
- [17] T. Photonics, *Active and passive stabilization of a high-power UV frequency-doubled diode laser*, (2023), URL: https://www.toptica.com/fileadmin/Editors_English/12_literature/01_quantum_technologies/toptica_Active_and_passive_stabilization_of_a_high-power_UV_frequency-doubled_diode_laser.pdf.
- [18] A. K. Mohapatra, T. R. Jackson, and C. S. Adams, *Coherent Optical Detection of Highly Excited Rydberg States Using Electromagnetically Induced Transparency*, Phys. Rev. Lett. **98** (11 2007) 113003.
- [19] T. Photonics, *Short, Shorter, Shortest: Diode Lasers in the Deep Ultraviolet*, (2023), URL: https://www.toptica.com/fileadmin/Editors_English/12_literature/01_quantum_technologies/toptica_Short_shorter_shortest_Diode_lasers_in_the_deep_ultraviolet.pdf.
- [20] M. G. Littman and H. J. Metcalf, *Spectrally Narrow Pulsed Dye Laser without Beam Expander*, Applied Optics **17** (1978) 2224.
- [21] T. F. Gallagher, *Rydberg Atoms*, Cambridge University Press, 1994.
- [22] S. Germer, *Frequency stabilization of a laser and a high resolution optical setup for excitation of ultracold Rydberg atoms*, Bachelor's thesis, 2023, URL: <https://www.nqo.uni-bonn.de/publications/publications/2023-samuel-germer-bachelor.pdf>.
- [23] K.-J. Boller, A. Imamoglu, and S. E. Harris, *Observation of electromagnetically induced transparency*, Phys. Rev. Lett. **66** (20 1991) 2593.
- [24] A. Vylegzhanin et al., *Excitation of ^{87}Rb Rydberg atoms to nS and nD states ($n68$) via an optical nanofiber*, Optica Quantum **1** (2023) 6.
- [25] R. W. P. Drever et al., *Laser phase and frequency stabilization using an optical resonator*, Applied Physics B **31** (1983) 97.
- [26] E. D. Black, *An Introduction to Pound–Drever–Hall Laser Frequency Stabilization*, American Journal of Physics **69** (2001) 79.
- [27] J. A. Boyd and T. Lahaye, *A basic introduction to ultrastable optical cavities for laser stabilization*, American Journal of Physics **92** (2024) 50.
- [28] M. J. Martin et al., “High-Precision Laser Stabilization via Optical Cavities,” *Optical Coatings and Thermal Noise in Precision Measurement*, United Kingdom: Cambridge University Press, 2012 237.

Bibliography

- [29] *Integriert-Optische Modulatoren (IOM)*, Accessed: January 14, 2025, Jenoptik, URL: <https://www.jenoptik.de/produkte/optoelektronische-systeme/lichtmodulation/integriert-optische-modulatoren-iom>.
- [30] Y. Li, M. Sun, T. Miao, and J. Chen, *Towards High-Performance Pockels Effect-Based Modulators: Review and Projections*, *Micromachines* **15** (2024) 865.
- [31] A. Boes et al., *Lithium niobate photonics: Unlocking the electromagnetic spectrum*, *Science* **379** (2023) eabj4396.
- [32] Murphy, *Integrated Optical Circuits and Components: Design and Applications*, Illustrated, vol. 66, *Optical Science and Engineering*, CRC Press, 1999 468, ISBN: 0824775775, 9780824775773.
- [33] W. Technologies, *SynthUSB3: RF Signal Generator for 12.5 MHz - 6.4 GHz*, 2023, URL: <https://windfreaktech.com/product/synthusb3-6ghz-rf-signal-generator/>.
- [34] *Phase and Frequency Locking of Diode Lasers: Error Signal Generation - Locking to a Reference Resonator*, Accessed: January 14, 2025, Toptica Photonics, URL: <https://www.toptica.com/application-notes/phase-and-frequency-locking-of-diode-lasers/error-signal-generation/locking-to-a-reference-resonator>.
- [35] S. M. Shinnars, *Modern Control System Theory and Design*, 2nd, Print, Place of publication not identified: J. Wiley, 1998.
- [36] S. Zacher, *Closed Loop Control and Management: Introduction to Feedback Control Theory with Data Stream Managers*, 1st, Springer International Publishing AG, 2023.
- [37] TOPTICA Photonics AG, *PID Feedback Controllers*, <https://www.toptica.com/application-notes/phase-and-frequency-locking-of-diode-lasers/pid-feedback-controllers>, Accessed: 2025-01-14, n.d.
- [38] Thorlabs, Inc., *Broadband Polarizing Beamsplitter*, https://www.thorlabs.com/newgrouppage9.cfm?objectgroup_id=739, Accessed: 2025-01-17, n.d.
- [39] TOPTICA Photonics AG, *FALC pro: Fast Analog Linewidth Control*, <https://www.toptica.com/products/laser-rack-systems/laser-locking-electronics/falc-pro>, Accessed: 2025-01-14, n.d.
- [40] D. Goldovsky, V. Jouravsky, and A. Pe'er, *Simple and robust phase-locking of optical cavities with > 200 KHz servo-bandwidth using a piezo-actuated mirror mounted in soft materials*, *Optics Express* **24** (2016) 28239.
- [41] T. C. Briles, D. C. Yost, A. Cingöz, J. Ye, and T. R. Schibli, *Simple piezoelectric-actuated mirror with 180 kHz servo bandwidth*, *Optics Express* **18** (2010) 9739.
- [42] Y.-X. Chao et al., *Pound–Drever–Hall feedforward: laser phase noise suppression beyond feedback*, *Optica* **11** (2024) 945.
- [43] B. E. A. Saleh and M. C. Teich, *Fundamentals of Photonics*, 3rd, Newark: Wiley, 2019.

Bibliography

- [44] M. Bhowmick, ed.,
Optical Interferometry: A Multidisciplinary Technique in Science and Engineering,
London: IntechOpen, 2022.
- [45] K. P. Zetie, S. F. Adams, and R. M. Tocknell, *How does a Mach-Zehnder interferometer work?*
Physics Education **35** (2000) 46.
- [46] W. Demtröder, *Electrodynamics and Optics*, 1st, Cham: Springer International Publishing, 2019.
- [47] X. Xie et al.,
Phase noise characterization of sub-hertz linewidth lasers via digital cross correlation,
Optics Letters **42** (2017) 1217.

List of Figures

2.1	The TASHG pro system from [15] is illustrated. The seed light provided by the DLpro laser at 960 nm passes an optical isolator to prevent back reflections to the laser. Then it is guided through a TA and is then frequency doubled to 480 nm. After beam shaping optics, the light can be used in the experiment.	4
2.2	The ladder scheme of ^{87}Rb adapted from [24]. The excitation from the ground state ($5S_{1/2}$) to the intermediate state ($5P_{3/2}$) is done with the 780 nm probe laser. Afterwards the Rydberg excitation is done with a 480 nm control laser.	6
3.1	At the top one can see the reflection signal of the light with the resonance dips being spaced out in $\Delta\nu_{\text{FSR}}$ and the width is given by $\Delta\nu_{\text{FWHM}}$. The respective phase signal can be seen at the bottom which has a zero-crossing at resonance and a steep slope around resonance [28].	9
3.2	Overview of a possible setup and the error signal generated from the PDH method. . .	11
3.3	Functional block diagram of a closed loop control [36]. Here, the set point w_{SP} is used as reference. Any difference will be given as control error e to the controller, which then gives a command y to the actuator. Outer disturbances z , like noise, is also taken into account. Through a sensor a feedback x_{feedback} is given and compared to the the current processes value x_{PV} and its deviation from the set point.	13
3.4	Setup after the 960 nm beam exits the laser system. First, the light passes through a half waveplate to ensure correct polarization before its hits a polarizing beamsplitter. The s component is reflected and couples into a fiber which is connected to a wavemeter. The p component is transmitted to the EOM fiber. In front of the EOM fiber an alignment of a half and quarter waveplate further guarantee correct polarization for the EOM fiber. .	16
3.5	Setup in front of the cavity. The beam passes through a polarizing beamsplitter and the transmission is guided by mirrors towards another PBS, where it is reflected to the cavity. The reflection from the cavity is going back until it hits the first PBS again and the power is detected with a photodiode, where the error signal can be extracted. The transmission of the cavity can also be measured with a PD after the cavity and the transverse modes can be viewed with a camera.	17
3.6	Transverse modes in the cavity viewed with a camera in transmission.	18
3.7	Transmission of the cavity measures with a photodiode (a) without and (b) with windfreak. In the first case one can see the transmission peaks of the ground-mode, whereas the high-order modes are barely visible. In the second case the sidebands are created with windfreak causing a lower power of the ground mode and additional resonances.	19

List of Figures

3.8	PDH Error signal measured while scanning the laser on the 11/27/2024. One can see the steep slopes at the lock points, i.e. at resonance and the two crossings at the sides of the steep slope. These are the zero crossings caused by the resonances of the sidebands. . .	20
3.9	Measurements taken with the spectrum analyzer for different control parameters (Tab. 3.1) and the corresponding bode plots and phase shift plots. The servo bump as well as the bode plots and phase shift plots have different characteristics depending on the chosen parameters.	21
3.10	Second measurements taken with the spectrum analyzer for different control parameters (Tab. 3.2) and the corresponding bode plots and phase shift plots. The servo bump as well as the bode plots and phase shift plots have different characteristics depending on the chosen parameters.	22
4.1	Setup of the MZI. The input light is split into two optical arms by an PBS and one arm is delayed with an fiber. Afterwards they come together on the BS and hit a PD, where the interference signal is detected. The PD also gives feedback with a PID controller to the piezo mirror in the delayed arm in case of drifts.	26
4.2	Signals of the PD visualized with an oscilloscope and terminated with $50\ \Omega$. The yellow signal corresponds to the PD signal and the green signal corresponds to the monitor signal of the lock box. (a) shows the transmission signal while scanning and (b) shows the signals locked to the slope of the transmission signal. In addition, a calibration of the transmission signal (c) was done.	27
4.3	Frequency noise measured with the network analyzer. Parameters: 10 averages, 3 decades and $1\ \text{M}\Omega$ termination. The measurements were done with the first PID parameters in table 3.1. (a) Raw spectrum of the frequency noise. The green data is the background, the blue the locked case and orange the unlocked. (b) Frequency noise with the background subtracted. The blue data represents the locked data and orange the unlocked. (c) Frequency noise converted to Hz^2/Hz	28
4.4	Frequency noise spectrum measured with the LeCroy. The first plot shows the background (red), the unlocked data (blue) and the locked data (green). In the second plot the background is subtracted and in the last plot some corrections were made to erase the dips in the high-frequency regime. The measurements were done with the first PID parameters in table 3.1.	29
4.5	Frequency noise measured with the network analyzer. Parameters: 10 averages, 3 decades and $1\ \text{M}\Omega$ termination. The measurements were done with the third PID parameters in table 3.2. (a) Raw spectrum of the frequency noise. The green data is the background, the blue the locked case and orange the unlocked. (b) Frequency noise with the background subtracted. The blue data represents the locked data and orange the unlocked. (c) Frequency noise converted to Hz^2/Hz	30
4.6	Frequency noise spectrum measured with the LeCroy. The first plot shows the background (red), the unlocked data (blue) and the locked data (green). In the second plot the background is subtracted and in the last plot some corrections were made to erase the dips in the high-frequency regime. The measurements were done with the third PID parameters in table 3.2.	31
4.7	Comparison of the LeCroy measurements of RQO control laser and HQO TASHGpro2.	32

List of Tables

3.1 Settings for the different parameters in the plots of figure 3.9 20

3.2 Settings for the different parameters in the plots of figure 3.10 20